Astronomy & Astrophysics manuscript no. paper
September 8, 2009

Characterization of horizontal flows around solar pores from high-resolution time series of images

S. Vargas Domínguez,[1] A. de Vicente[2], J.A. Bonet[2] and V. Martínez Pillet[2]

[1] Mullard Space Science Laboratory, University College London, Holmbury, St Mary, Dorking, RH5 6NT, UK
e-mail: svd@mssl.ucl.ac.uk
[2] Instituto de Astrofísica de Canarias, 38205 La Laguna, Tenerife, Spain

Received September 8, 2009; accepted month day, 2009

ABSTRACT

Context. Though there is increasing evidence linking the moat flow and the Evershed flow along the penumbral filaments, there is not a clear consensus regarding the existence of a moat flow around umbral cores and pores, and the debate is still open. Solar pores appear to be a suitable scenario to test the moat-penumbra relation as evidencing the direct interaction between the umbra and the convective plasma in the surrounding photosphere, without any intermediate structure in between.
Aims. The present work studies solar pores based on high resolution ground-based and satellite observations.
Methods. Local correlation tracking techniques have been applied to different-duration time series to analyze the horizontal flows around several solar pores.
Results. Our results establish that the flows calculated from different solar pore observations are coherent among each other and show the determinant and overall influence of exploding events in the granulation around the pores. We do not find any sign of moat-like flows surrounding solar pores but a clearly defined region of inflows surrounding them.
Conclusions. The connection between moat flows and flows associated to penumbral filaments is hereby reinforced by this work.

Key words. Sun: activity – Sun: photosphere – Sun: granulation

1. Introduction

The solar photosphere displays a wide variety of magnetic features at different spatial scales being sunspots and pores the more conspicuous ones. The morphology and evolution of sunspots and pores have been extensively studied and both are thought to be ruled by the mutual effect of magnetic field that inhibits convection (though not completely) and plasma motions. Nevertheless, there is not clear consensus for a model explaining the transition from pores into sunspots (i.e. development of penumbra, see the monograph by Thomas & Weiss (2008)), the fade of the Evershed flow once leaving the penumbra and entering the region dominated by the large outflows (the so-called moat flows), the flow patterns surrounding pores which are, alternatively, dominated by downflows surrounding them (Giordano et al., 2008) or moat-like flows (Zuccarello et al., 2009) and, also, the effect of the penumbra in the granular pattern surrounding sunspots.

By using local correlation tracking techniques Vargas Domínguez et al. (2007) found a direct correlation between the presence of penumbrae and the appeareance of moat flows in a complex δ-configuration active region. A more extensive sample taking into account different penumbral configurations was analyzed by Vargas Domínguez et al. (2008), establishing a systematic moat-penumbra relation in all the sunspots under study. According to these studies, no moat flow was detected in the granulation next to umbral boundaries lacking penumbrae. Moat flows were always detected as a prolongation of the penumbral filaments once crossing the penumbral boundary.

Though there is increasing evidence linking the moat flow and the Evershed flow along the penumbral filaments (e.g. Sainz Dalda & Martínez Pillet, 2005; Cabrera Solana et al., 2006), the debate regarding the existence of a moat flow around umbral boundaries without penumbra and individual pores is still ongoing. In a recent work, Deng et al. (2007), found that the dividing line between radial inward and outward proper motions in the inner and outer penumbra, respectively, survived the decay phase, suggesting that the moat flow is still detectable after the penumbra disappeared. However, previous works (Sobotka et al., 1999; Roudier, Bonet & Sobotka, 2002; Hirzberger, 2003) have measured horizontal proper motions in and around pores and have observed some penetrating flows at the umbral boundaries and a ringlike arrangement of positive divergences (*rosettas*) around the pores which is related to a continuous activity of exploding granules in the granulation around them. Roudier, Bonet & Sobotka (2002) identified a very clear inflow around pores which corresponds to the penetration of small granules and granular fragments from the photosphere into the pores, pushed by granular motions originated in the divergence centres around them. These authors conclude that the motions at the periphery of the pore are substantially and continuously influenced by the external plasma flows deposited by the exploding granules. It is important to note in this context that the annular area surrounding pores and filled with exploding granules generates an outward directed flow annulus that can give the impression of a persistent outflow.

Pores are interesting to analyze since, as they do not display penumbrae (Keil, 1999), what we actually observe is the direct

interaction between the umbra (with a strong vertical magnetic field that inhibits convection inside it) and the convective plasma in the surrounding photosphere, without any intermediate structure in between. Many observed features such as bright granules moving in the border of a pore (Sobotka et al., 1999) show the complex exchange taking place between the pore and its surrounding granulation.

Our main interest is the characterization of the horizontal flows around a variety of solar pores on the basis of high-resolution time series of images. Observations from ground-based and space telescopes are analyzed by means of the local correlation tracking technique. In Sect. 2, the paper concentrates on the description of the images acquisition and data processing separately for ground-based and satellite data. The analysis of the data and the presentation of results are treated in Sect. 3. A general summary and final discussion are presented in Sect. 4.

2. Observations and data processing

A significant part of our data were acquired during a long observing campaign (24 days) carried out in September-October 2007 with the cooperation of several European and Japanese institutions and joint observations from several solar telescopes of the Canary Islands Observatories: SST and DOT in La Palma and VTT and THEMIS in Tenerife. Moreover, and for the very first time, coordinated observations with the space solar telescope *Hinode* (Kosugi et al., 2007) were performed in the framework of the *Hinode Operation Program 14*. In the next sections, we will detail the ground-based and satellite observations supporting the present work as well as the specific data processing applied in each case.

2.1. Ground-based SST data

The data from the Swedish 1-m Solar Telescope (SST, Scharmer et al., 2003a,b) analyzed in the present work were recorded during a particular observing run on 30 September 2007 and correspond to the active region NOAA 10971. The main target was a region close to the solar disc center (μ=0.98) with some pores of different sizes embedded in a plage region that exhibits an intense magnetic activity.

A dichroic beam-splitter in the optical setup divided the light beam into two channels: blue and red. Images in G-band (λ4305.6 Å) and CaII H (λ3969 Å) were acquired in the blue beam at a rate of 13 frames s^{-1}. We used 12 bit detectors of 2048 $\times$ 2048 square pixels which in combination with an image-scale of 0.034 arcsec/pix rendered an effective field-of-view (hereafter FOV) of 69 $\times$ 69 square arcsec. After dark current subtraction and flatfielding, G-band and CaII H images were independently corrected for atmospheric and instrumental degradation by employing the so-called *Multi-Frame Blind-Deconvolution* restoration technique (MFBD, Löfdahl, 1996, 2002). For each wavelength, the image sequence was grouped in sets of about 80 consecutive frames acquired within time intervals of 10 seconds each. Every set yielded one restored image. From $\sim$ 52640 single exposures in G-band and as many in CaII H we obtained a total of 658 restored images per wavelength. Next steps in the data post-processing were: compensation for diurnal field rotation, rigid alignment of the images, correction for distortion and finally subsonic filtering. For more details see Vargas Domínguez (2008).

The red beam fed the filter *Solar Optical Universal Polarimeter* (SOUP, Title et al, 1986) to obtain Hα (λ6562.8 Å) and narrow-band images at 6302 Å. Single images were taken at a rate of 35 frames s^{-1} with CCDs of 1024 $\times$ 1024 square pixels and an image-scale of 0.065 arcsec/pix. A beam splitter in front of the SOUP deflected a fraction of light to obtain simultaneous broad-band Phase Diversity image-pairs in the continuum near λ6302 Å. These images made up an additional *object* for the *Multi-Object Multi-Frame Blind-Deconvolution* (MOMFBD, Van Noort, Rouppe van der Voort & Löfdahl, 2005) algorithm to jointly restore both, the broad-band and the narrow-band images. From the restored narrow-band images, we computed longitudinal magnetograms and dopplergrams.

Due to periods of bad seeing in which the quality did not reach the desired top level, some of the images were discarded and we kept only the best and longest consecutive sequence of images. The very final product were 4 time series (2 for G-band, 2 for CaII H) with the characteristics listed in Table 1. The time gap of about 5 min between the two consecutive series for each wavelength resulted from a telescope tracking interruption. That is also the reason why the FOV is slightly different in both time series. Most images forming the time series show details near the diffraction limit of the telescope. Figure 1 displays one of the best quality G-band restored images with close-ups enhancing very tiny bright features in the intergranular lanes.

The procedure followed for image restoration is extensively detailed in Vargas Domínguez (2008). Figure 2 shows one of the co-temporal sets of images of the emerging active region after restorations.

2.2. Hinode space satellite data

After launched on 22 September 2006, *Hinode* has become an extremely successful observatory for Solar Physics research. It has managed to observe many high-detailed solar features by avoiding the blurring and distortion effects produced by the Earth's atmosphere. The public archive of *Hinode*[1] is an organized data base where all *Hinode* observations can be found out and easily downloaded.

We were interested in *Hinode* observations of solar pores taken with the Solar Optical Telescope (SOT, Tsuneta et al., 2008), in order to pursue our study of photospheric horizontal flows. Next two sections describe the *Hinode* data we analyze in this paper. These data extend the sample of cases under study in the present work and moreover give us the possibility to compare with the results stemming from ground-based observations.

2.2.1. Data from 1st June 2007

These data correspond to a solar portion including an isolated and round-shaped pore observed by *Hinode* on 1st June 2007. Images were acquired in G-band with a cadence of 30 seconds in

[1] See the website: *http://solar-b.nao.ac.jp/hsc_e/darts_e.shtml*

Table 1. Characteristics of the time series of solar pores observed from ground-based and satellite facilities.

Telescope	Date 2007	Series	Time, UT	Duration [min]	N. images	Cadence [sec]	FOV [″]
SST ...	30 Sep ...	1	08:43-09:31	48	286	10	64.3×65.0
		2	09:36-09:56	20	118	10	64.3×65.0
Hinode ...	1 Jun ...	1	21:35-21:55	20	40	30	27.9×55.7
		2	22:26-23:33	67	134	30	27.9×55.7
	30 Sep ...	1	00:14-17:59	960	1030	60	55.7×111.4

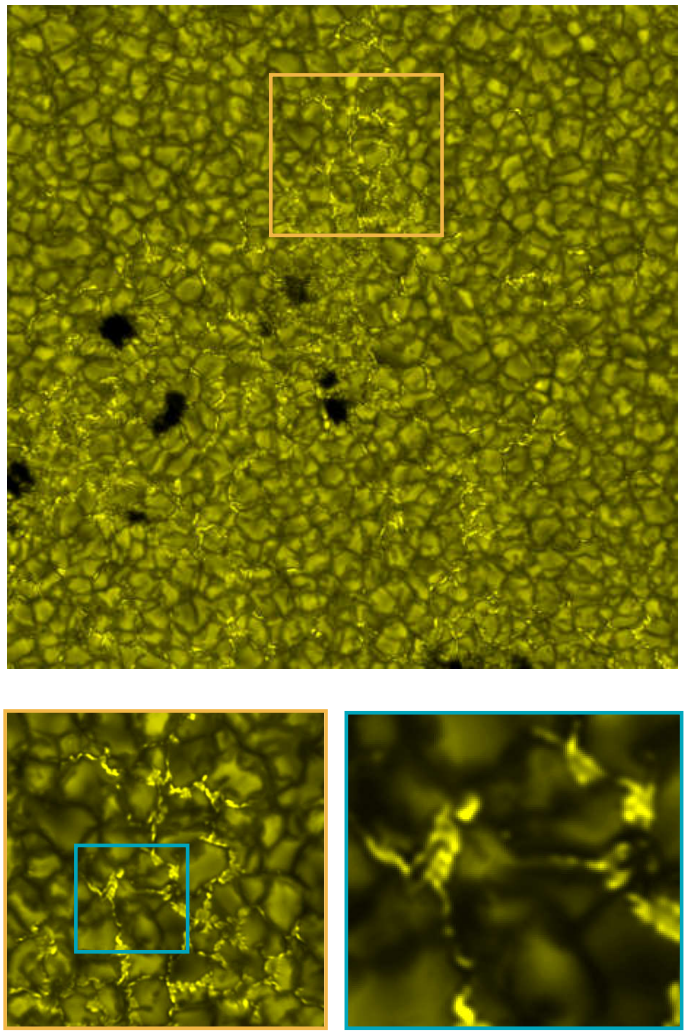

Fig. 1. G-band restored image (false color) of the emerging active region on 30 September 2007. Small colored boxes are close-ups showing the high-resolution reached after the restoration process that enable us to detail very tiny structures in the bright features placed in the intergranular lanes. The size of the box in the lower right corner is 6.″4 × 5.″8.

a solar portion close to the disk center (μ=0.87). After subsonic filtering we obtained two time series; Table 1 (1 Jun) summarizes the parameters of both series in detail. The treatment performed with *Hinode* data does not include any restoration process because of their excellent quality as consequence of the absence of atmospheric turbulence.

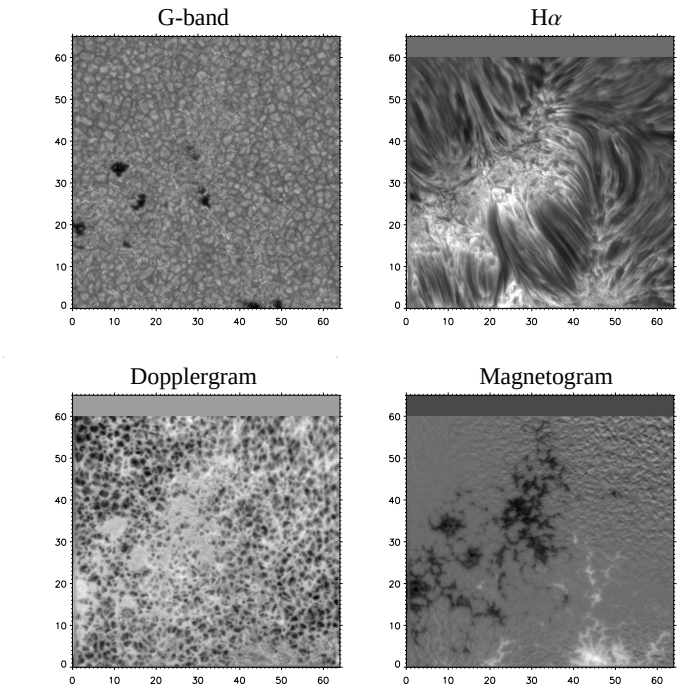

Fig. 2. SST Co-temporal and co-spatial set of images from the emerging flux region on 30 September 2007. The coordinates are expressed in arc sec.

2.2.2. Data from 30 September 2007

The data from *Hinode* on 30 September 2007 correspond to the coordinated observations described in Sect. 2.1. *Hinode* observed in G-band the emerging flux region NOAA 10971 during almost the whole day from 00:14 to 17:59 UT with a few brief interruptions for calibrations. Table 1 (30 Sep) summarizes the parameters of the time series in more detail. A significant part of the FOV in the SST images is covered by the *Hinode* observations.

Hinode data often presents misalignments due to tiny tracking flaws and also due to temporal interruptions. We proceeded by aligning all of the 1030 images (18 hours) at a sub-pixel level. Taking the first image as the reference, the following images were aligned by correlating pairs of subsequent images and accumulating their misalignments.

The next step in the reduction process was the subsonic filtering of the time sequence. Because of the short temporal interruptions in the series (a total of 7 during the 18 hours) we fragmented the whole series in 8 data cubes of about 130 images each so that consecutive images in every cube were equally spaced. Subsonic filtering was applied independently to every

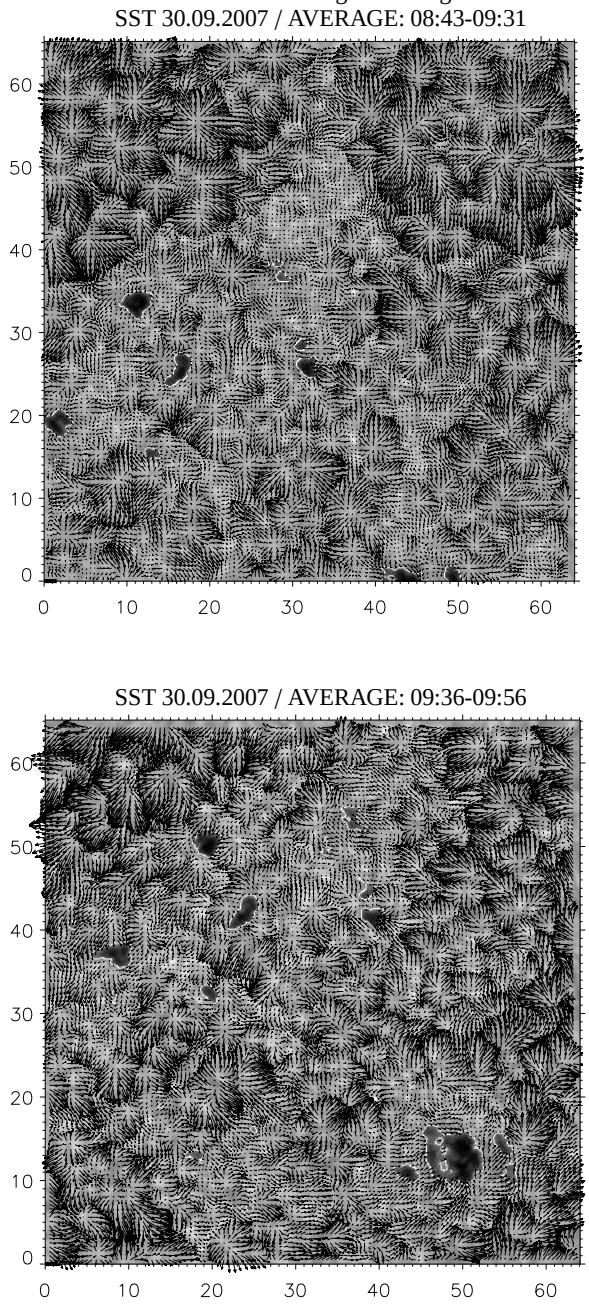

Fig. 3. Map of horizontal velocities (FWHM 1.″0) from the restored time series taken at the SST on September 30, 2007. The velocities are averaged over 48 minutes (*upper panel*) and 20 minutes (*lower panel*). The *white contours* outline the border of solar pores. The length of the black bar at coordinates (0,0) corresponds to 1.6 km s^{-1}. The coordinates are expressed in arc sec. The background in every case represents the average image of the corresponding G-band series.

cube.

3. Data analysis and results

3.1. General description of horizontal proper motions in the FOV

The G-band series taken at both SST and *Hinode* have been employed to analyze the horizontal proper motions of structures in every FOV, by using the local correlation tracking (LCT) technique (November & Simon, 1988) as implemented by Molowny-Horas & Yi (1994). In this section, we show the maps of horizontal velocities calculated for the different time series by using a Gaussian tracking window of FWHM 1.″0 which is roughly half of the typical granular size.

Figure 3 shows the flow maps computed from the two restored time series in the SST. The velocities were averaged over the total duration of each series. The underlying background in the maps is the average image of the respective series. As commented above, the FOV is slightly different in both cases so that, for instance, the pore at coordinates (17,26) in the upper map of the figure is located at (24,42) in the lower map.

The maps are dominated by flows coming from exploding events taking place all over the FOV. As expected, the map averaging over a longer time period (48 min) is slightly smoother than the other one (20 min), and displays lower velocities. Nevertheless, both maps reproduce similar flow patterns all over the FOV. The top of the FOV in Fig. 3 (*upper panel*) shows very conspicuous exploding granular events which are grouped at every upper corner of the FOV forming two large-scale structures that fit well the supergranular one (see also the magnetogram in Fig. 2). A smaller portion of these structures can also be identified in the lower panel of Fig. 3. Even though a complete description of the proper motions around the pores in the FOV will be done in Sect.3.5, a glance at the figure reveals no evidence of a moat-like pattern around any of the pores. The central part of the FOV where the smaller pores are embedded, exhibits a lower magnitude of horizontal velocities. This behavior is explained by the intense magnetic activity in this part of the FOV as unveiled by the corresponding magnetogram of the zone shown in Fig. 2.

Concerning *Hinode* data, the computed map of horizontal velocities for the time series of 1 June 2007 is displayed in Fig. 4. This map is calculated from the longest time series [2](67 minutes, see Table 1). The isolated solar pore is immersed in a granular region displaying several and recurrent large exploding granular events all around it. The main conclusions stemming from the analysis of SST data are also applicable here, i.e. the connection of the centers of the exploding events outlines a round-shaped contour at a distance from the pore border comparable to the pore diameter. Velocity magnitudes in the outer part of the outlined contour are clearly larger than those in the inner part between the contour and the pore border. The resulting map of horizontal velocities for 30 September 2008 data will be presented in Sect. 3.3 where we pursue a detailed analysis for this time series.

3.2. Averaging horizontal flows within different temporal windows

To study the influence of different time averages in the velocity maps we consider temporal windows of 5, 10, 15 and 20 min in the best quality G-band time series recorded at the SST (series 2 of 30 September in Table 1). As expected, the maps (not shown in the paper) are smoother for longer averaging periods.

[2] Analysis of the shortest series (not presented here) gives similar results though, as expected, noise and velocity magnitudes increase significantly.

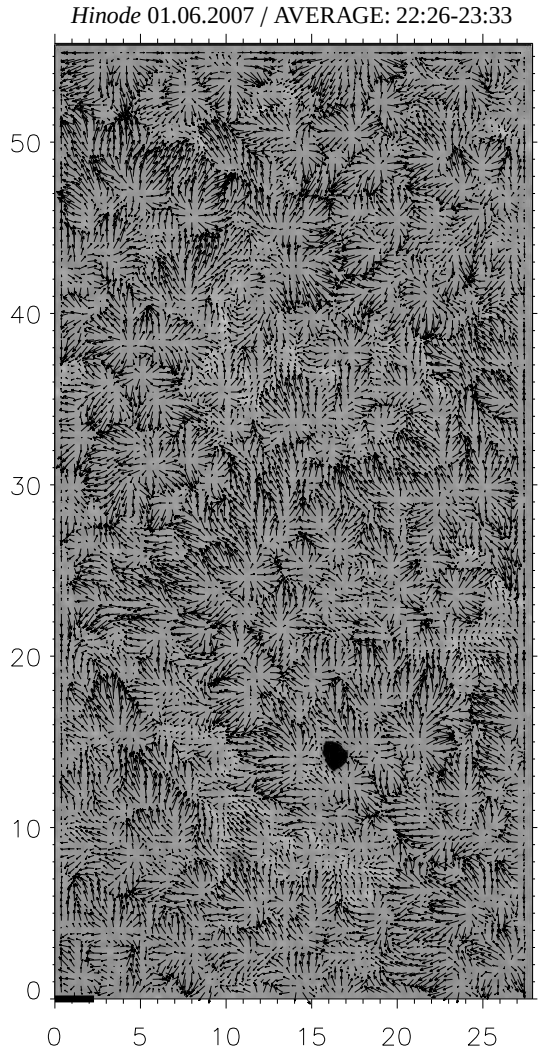

Fig. 4. Maps of horizontal velocities (FWHM 1.″0, 67 minutes average) for the processed time series taken by *Hinode* on June 1, 2007. The length of the black bar at coordinates (0,0) corresponds to 2.3 km s^{-1}. The coordinates are expressed in arc sec. The background represents the average image of the G-band series.

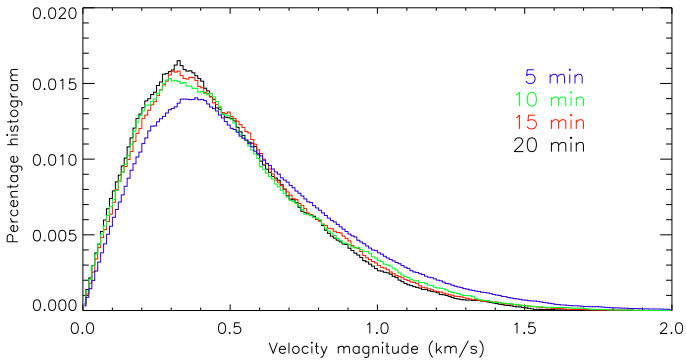

Fig. 5. Histogram of horizontal velocity magnitudes for different time intervals. A local correlation tracking technique has been used to derive the horizontal velocities (FWHM=1.″0).

Regardless of whether we average over 5 or 20 min intervals, we find essentially the same general trends with exploding granular patterns all over the FOV, meaning that the averaging periods we are employing are smaller than or about the lifetime of the observed structures. It is also worth emphasizing that we do not recognize any moat-like flow around the pores for such different time averages.

Figure 5 shows the histograms of the velocity magnitudes for each averaging temporal window considered. The resulting distribution is very similar in the four cases but the histograms shift to the left as the averaging period increases. Thus, the largest velocity magnitudes range from 1.83 to 1.97 km s^{-1} and the mean values from 0.48 to 0.50 km s^{-1}. In both cases, smaller/larger values correspond to longer/shorter time averages.

3.3. Long-term evolution of the velocity field

In order to investigate how the evolution of the emerging region affects the velocity in the FOV for long periods of time, we have used the *Hinode* time series lasting for several hours. *Hinode* data on 30 September 2007 corresponds to 18 hours of almost continuous solar observation as reported in Sect. 2.2.2. The stable good quality and long duration of the series is ideal to study the evolution of the flow maps in an emerging flux region. To that aim the images are grouped in 1-hour sets (from 00:14 UT up to the time 14:00 UT) and every set is processed independently resulting in 14 maps of horizontal velocities which are computed using a Gaussian tracking window of FWHM 1.″0. Fig. 6 shows, out of these fourteen maps, those corresponding to times: 1 hour after 00:14 UT, 5, 9 and 13 hours later, respectively [3].

The main pore is located in the spatial position (37,55) in the first map (Fig. 6) and surrounded by some smaller pores which form altogether a sort of vertical and elongated arrangement in the figure. The collection of these pores is evolving in time and some of them start merging and disappearing. The final picture of the region displayed in Fig. 6 shows the isolated main pore with only a very tiny magnetic companion.

We do not identify any signal of moat-like flow around the pores in any of the evolutionary stages shown in the maps sequence but continuous activity caused by exploding granules. Centers of divergence are systematically identified, some of them very close to the pore border. Proper motions displaying inward components are more common around the pores and **no** outward regular large-scale flow, as corresponding to a moat-flow, is found. These results are firmly validated because of the long duration of the sample and reinforce the previous analysis pursued for the only 1-hour long SST data in Sect. 3.1.

3.4. Distribution of horizontal speeds in the FOV

Figure 7 shows the location (*white areas*) of speeds (velocity magnitudes) within three different ranges in km s^{-1}, for the SST data (the first series in Table 1): low velocity magnitudes lower than 0.3, medium velocity magnitudes in the range 0.3 - 0.8 and

[3] A movie displaying the evolution of the pore throughout the 18-hour observation can be downloaded from the website *http://www.iac.es/proyecto/solarhr/hinode30sep2007.mov*

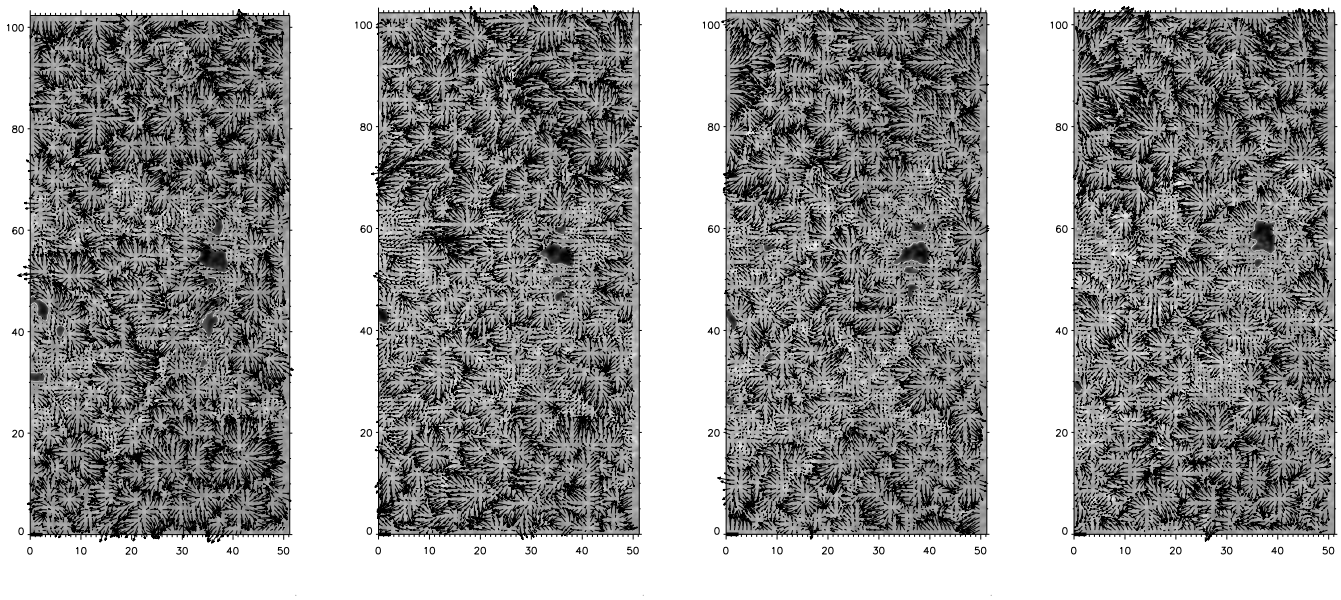

Fig. 6. Horizontal flows in a solar pores region observed with *Hinode* on 30 Sep 2007. Fourteen maps are produced, each one computed from data in 1-hour intervals. From left to right, it is shown the maps corresponding to intervals 1, 5, 9 and 13, respectively. The length of the black bar at coordinates (0,0) corresponds to 2.3 km s^{-1}. The coordinate are expressed in arc sec. The background represents the average image in every hour-set.

large velocity magnitudes greater than 0.8.

Small speeds are mainly grouped in the central part of the FOV where an intense magnetic activity is detected as evidenced by the high concentration of G-band bright points and faculae present in this region (see Figs. 1 and 2). Around pores, the velocity magnitudes mainly correspond to the lower range (< 0.3 km s^{-1}) so that they are surrounded by white areas in Fig. 7 (*upper panel*). The areas mapping medium velocity magnitudes are regularly spread out all over the FOV except in the proximity of pores (Fig. 7 *middle panel*). The shape of empty (*non white*) areas around the pores roughly reproduce the pores shape. Large velocities (> 0.8 km s^{-1}) are not homogeneously distributed in the FOV but mainly located in the two upper corners of Fig. 7 (*lower panel*) where the granulation is less-magnetized (see magnetogram in Fig. 2). These zones show large velocity flows that might reflect the presence of supergranular cells as commented in Sect. 3.1.

3.5. Velocity distribution around solar pores

From the computed velocity fields we can perform a detailed analysis of the velocity distribution around the solar pores. To pursue this study we will use the region observed with the SST where we have a useful collection of pores available to work with. As we have two time series for this region (see Table 1), we will employ the first one covering the longest time period, except for one of the pores which is out of the FOV. For this pore, we will use the second time series. Figure 8 shows the FOV including all the pores under study which are labeled with consecutive numbers for easy identification hereafter.

Figure 8 (*lower panel*) illustrates the projection of the velocities into radial and transversal components as a convenient way to compute inward and outward motions. The figure plots two points in the granulation surrounding a solar pore with their corresponding velocity vectors **v**. The pore is centered at coordinates (x_c, y_c) with respect to the orthogonal coordinate system X,Y placed at the lower left corner of the FOV. Vector **r** is the position vector of a given point with respect to the pore center. The pore center is located at its gravity-center calculated by weighting the position of every point inside the pore with the inverse of its respective intensity. Velocity vectors in every point of the granulation surrounding the pore are projected into radial v_r and transversal v_t components.

In order to establish the inward and outward motions, we first select the FOV including the pore under study. Since active regions in general, and pores in particular, exhibit their own displacement (due to differential rotation and intrinsic motions) while embedded in the granulation pattern, we align the time series with respect to an area framing the pore (correlation box) so that we make sure we are measuring plasma motions with respect to the pore. We compute the map of horizontal velocities by LCT with the same Gaussian tracking window (FWHM 1.″0) employed in the previous sections. The next step is to define the "radial directions" (see lower panel in Fig. 8) that will be used as the reference to project the velocities. For short distances these directions are defined as perpendicular to the pore border. These perpendicular directions are calculated from the gradients of intensity in a smoothed pore-mask image[4]. This way, one can also deal with non round-shaped pores. The limit for short distances is defined by thresholding the intensity gradients. The threshold depends on the pore shape and size. At large distances (i.e. ∼3 times larger than the pore mean radius) all pores are considered as round-shaped structures and the radial directions are defined by the position vector **r** of a given point with respect to the pore center. According to the lower panel in Fig. 8, inward/outward motions correspond to $\cos\beta$

[4] A binary mask setting the area occupied by the pore (1/0 inside/outside the pore) is defined. Then this mask is smoothed by convolving with a Gaussian function so that we obtain a distribution of pseudo-intensities smoothly ranging from 1 to 0 and describing a blurred shape of the pore. This will be the smoothed pore-mask image to which we refer above.

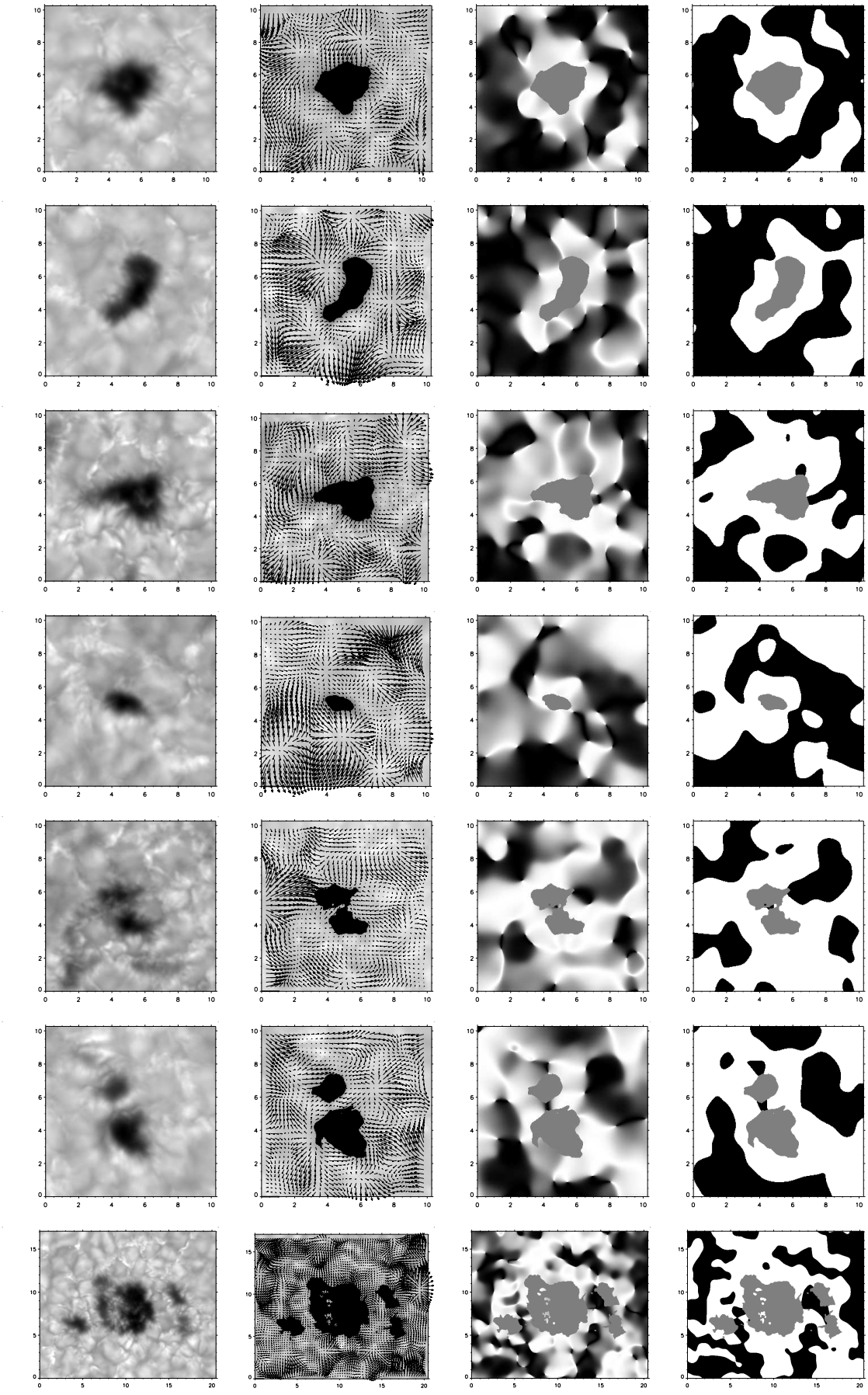

Fig. 9. Discrimination between inward and outward motions surrounding solar pores displayed in Fig. 8 (*upper panel*). Rows display pores from 1 to 7 (*top to bottom*) and the four columns correspond to (*left to right*): the average image of the time series, the map of horizontal velocities, the map of $\cos\beta$ and the binary map of inward (*white*) and outward (*black*) radial velocities. See the text for details. The spatial units are in arc sec.

negative/positive, where β is the angle formed by **v** and the positive radial direction (outward) at each point of the FOV. The value of $\cos\beta$ is mapped in gray scale ranging from 1 for purely radial outward velocities (*in black*) to -1 for purely inward velocities (*in white*). A binary mask is created from the previous gray-scaled map where areas in *black* and *white* correspond to velocities with positive (outward) and negative (inward) radial components, respectively.

We apply the aforementioned method to our sample of 7 different pores shown in the upper panel of Fig. 8. The results are displayed in Fig. 9 where rows display the different pores and the columns correspond to: 1) the averaged FOV around the pore; 2) the velocity field; 3) the gray-scale representation of $\cos\beta$; and 4) the final binary representation mapping the areas with inward (*white*) and outward (*black*) radial velocity components, after applying the binary mask. The analysis of all cases establishes that the flows display a clear preference for inward directions around the pores. This fact is systematically found in all examples. The more regular-shaped pores are surrounded by an also regular annular-like area with inward velocity components, having a mean width similar to the center-to-border distance in the pore. The dividing line between inward and outward motions is connecting the centers of divergence.
Fig. 10 (upper panels) shows color-scaled maps of the velocity magnitudes (ranging from 0 to 1 km s^{-1}) for the more regular-shaped pores (1 and 2) in our sample, represented in the the two upper rows of Fig. 9. Note that both pores exhibit proto-penumbral structures which are also visible in other pores of the sample. The centers of divergence are clearly identified in the maps of Fig. 10 as *black structures* around the pores. Another important distinctive feature in these maps is that the highest speeds are located beyond these black structures away from the pore.

In an attempt to study a possible systematic trend in the variation of the speeds around the pores, we calculate the mean velocity magnitude in consecutive ribbons (strips) encircling the pores 1 and 2. A total of 12 adjacent ribbons ($\sim 0\farcs24$ wide), referred to as ring-like structures surrounding the pore, are used for this analysis.

Figure 10 (*lower panels*) plots the speeds versus distance to the pore border. The velocity magnitudes increment as a function of this distance: 1) the mean value of speeds increments rapidly at distances ranging from $\sim 0\farcs15$ to $0\farcs4$; 2) in the range $0\farcs4$ - $1\farcs0$ the variation curve is flatter; 3) in the range $1\farcs0$ - $1\farcs6$ we again obtain very sharp increments. Up to this distance from the pore border, we observe the same behavior in both pores. Nevertheless, the mean speed values at $1\farcs6$ are quite different (250 vs. 390 m s^{-1}). At further distances ($> 1\farcs6$) the trend in the mean velocity magnitudes differs substantially. We must bear in mind that the flows around the pore can also be affected by the intrinsic characteristics of every single pore and by the contribution from other sources in the neighbourhood, e.g. pores in the vicinity.

4. Discussion

The proper motions in solar active regions displaying pores are analyzed from high-resolution time series of images. The observing material stems from coordinated ground-based and space observations. Thus, part of this material was acquired with the Swedish 1-m Solar Telescope, and reconstructed by employing the novel MFBD and MOMFBD techniques to achieve image resolutions near the diffraction limit. The other part of the data stems from the solar telescope on board the *Hinode* satellite. The long duration, stability and high-resolution of the time series achieved by *Hinode* enable us to study dynamical properties of the photospheric horizontal flows along periods of time much longer than those typically reachable from ground-based observations which are restricted by varying seeing conditions.

The local correlation technique applied to the time series allowed us to track the proper motions of structures in solar active regions and particularly in the areas nearby solar pores. Proper motions have been tracked in a variety of active regions for periods of typically 20-60 min but also one for several hours. We conclude that the flow patterns derived from different observational sets are consistent among each other in the sense that they show the determinant and overall influence of exploding events in the granulation around the pores and in the whole FOV. Motions toward the pores in their nearest vicinity are the dominant characteristic we claim to observe systematically. Thus, we do not find any trace of moat flow in the wide sample of pores studied. The motions at the periphery of the pores are basically influenced by the external plasma flows deposited by the exploding events, as suggested by other authors in previous works (Sobotka et al., 1999; Roudier, Bonet & Sobotka, 2002) In addition, the magnitude of the horizontal velocities is attenuated in the more magnetized areas of the FOV and particularly around the pores.

We interpret the dividing line between radial inward and outward motions, found by Deng et al. (2007) outside the residual pore in the last stage of a decaying sunspot, as corresponding to the location of the centres of divergence of the exploding events around the pore. The outward motions these authors describe, which are not in the immediate surroundings of the pore but separated by the annular inward motion, would then correspond not to moat flows but to the outward flows originated in the regular mesh of divergence centers around the pore.

Acknowledgements. The Swedish 1-m Solar Telescope is operated in the island of La Palma by the Institute of Solar Physics of the Royal Swedish Academy of Sciences in the Spanish Observatorio del Roque de los Muchachos of the Instituto de Astrofísica de Canarias. We thank the scientists of the *Hinode* team for the operation of the instruments. *Hinode* is a Japanese mission developed and launched by ISAS/JAXA, with NAOJ as domestic partner and NASA and STFC (UK) as international partners. It is operated by these agencies in co-operation with ESA and NSC (Norway). The reconstruction of images using the MOMFBD technique is a very computationally expensive task. To reduce the time needed for it, we made use of the Condor workload management system (http://www.cs.wisc.edu/condor/). S. Vargas thanks the people from the Institute of Solar Physics in Stockholm for his support during his short-stay in Sweden. Partial support by the Spanish Ministerio de Ciencia e Innovación through projects ESP2006-13030-C06-01 and AYA2007-63881, and financial support by the European Commission through the SOLAIRE Network (MTRN-CT-2006-035484) are gratefuly

References

Cabrera Solana, D., Bellot Rubio, L.R., Beck, C., Del Toro Iniesta, J.C., 2006, ApJ 649, L41
Deng, N., Choudhary, D.P., Tritschler, A., Denker, C., Liu, C., & Wang, H., 2007, ApJ 671, 1013-1021
Giordano, S., Berrilli, F., Del Moro, D., Penza, V., 2008, A&A, 489, 747
Hirzberger, J., 2003, A&A, 405, 331
Keil, S. L., Balasubramaniam, K. S., Smaldone, L. A., & Reger, B. 1999, ApJ, 510, 422

Kosugi, T., Matsuzaki, K., Sakao, T., et al. 2007, Sol. Phys., 243, 3
Löfdahl, M.G. 1996, Ph.D Thesis, Stockholm University, Stockholm (Sweden)
Löfdahl, M.G., 2002, Proc. SPIE., 4792, P.146
Molowny-Horas, R., & Yi, Z., 1994, ITA (Oslo) Internal Rep. No. 31
November, L.J., & Simon, G.W., 1988, ApJ 333, 427
Roudier, Th., Bonet, J.A., & Sobotka, M., 2002, A&A, 395, 249
Sainz Dalda, A., Martínez Pillet, V., 2005, ApJ, 662, 1176
Scharmer G. B., Bjelksjö K., Korhonen, T.K., Lindberg, B. & Petterson, B., 2003a, Proc. SPIE. 4853, 341
Scharmer G. B., Dettori, P. M., Löfdahl, M.G. , & Shand, M. 2003b, Proc. SPIE, 4853, 370
Sobotka, M., Vázquez, M., Bonet, J.A., Hanslmeier, A., Hirzberger, J., 1999, ApJ, 511, 436
Thomas, J.H. & Weiss, N.O., 2008 in Sunspots and Starspots, Cambridge Astrophysics Series 46, CUP, Cambridge
Title, A. M., Tarbell, T. D., Simon, G., and the SOUP team. 1986, Adv. Space Res., 6,253
Tsuneta, S., et al. 2008, Sol. Phys., 249, 167
Van Noort. M., Rouppe van der Voort, L., Löfdahl, M. G., 2005, Sol. Phys., 228, 191
Vargas Domínguez, S., Bonet, J.A., Martínez Pillet, V., Katsukawa, Y., Kitakoshi, Y., Rouppe van der Voort, L., 2007, ApJL, 660, L165
Vargas Domínguez, S., Rouppe van der Voort, L., Bonet, J.A., Martínez Pillet, V., van Noort, M., Katsukawa, Y. 2008, ApJ, 679, 900
Vargas Domínguez, S., 2008, PhD thesis, University of La Laguna - Instituto de Astrofísica de Canarias, Tenerife (Spain)
Zuccarello, F., Romano, P., Guglielmino, S.L., Centrone, M., Criscuoli, S., Ermolli, I., Berrilli, F., Del Moro, D., 2009, A&A, 500, L5

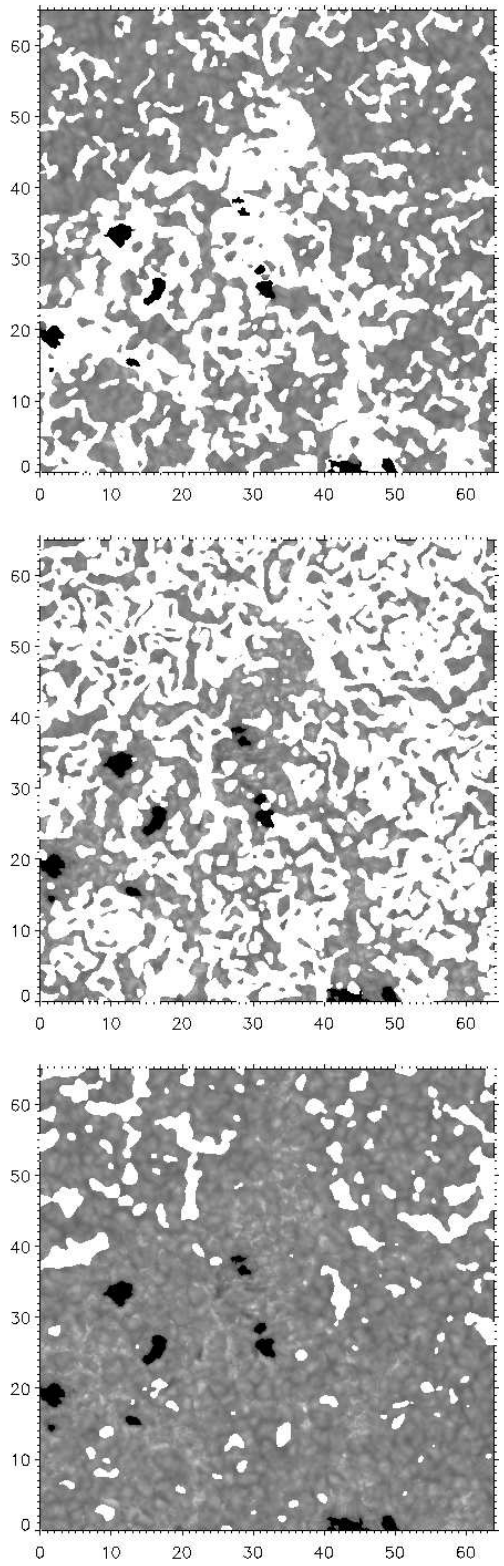

Fig. 7. Location of the areas (*in white*) where the magnitude of horizontal velocities is lower than 0.3 km s^{-1} (*upper panel*), between 0.3 - 0.8 km s^{-1}(*middle panel*) and greater than 0.8 km s^{-1}(*lower panel*). Pores are colored in black. The coordinates are expressed in arc seconds.

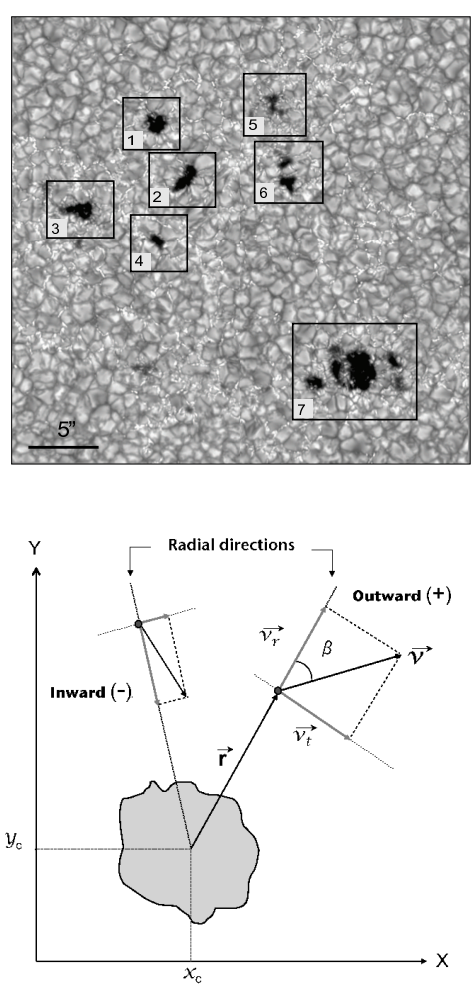

Fig. 8. *Upper panel*: emerging active region observed with the SST on 30 September 2007. *Lower panel*: sketch showing the projection applied to the velocities around a solar pore centered at (x_c, y_c) respect to the orthogonal coordinate system X, Y. The figure shows the velocity vectors **v** for two points in the granulation region around the pore (*small black dots*). The projection of **v** along the radial and transversal directions renders the radial v_r and transversal v_t velocity components, respectively.

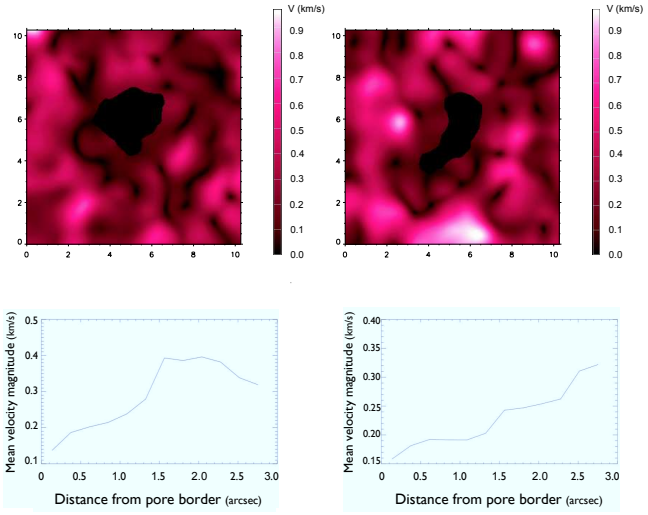

Fig. 10. Analysis of the velocity magnitudes of proper motions around solar pores. *Upper panel*: magnitude of horizontal velocities in false-color representation. *Lower panel*: plot of the mean velocity magnitude versus the distance from the pore border. The spatial units are in arc sec.